Journal of Materials Science & Technology 283 (2027) 182–190

Contents lists available at ScienceDirect

Journal of Materials Science & Technology

journal homepage: www.elsevier.com/locate/jmst

Research Article

Laminated passivation film in $Ti_2(Al_{1-X}Sn_X)C$ coatings via Sn-mediated selective oxidation for enhanced corrosion resistance in PEMFCs

Jingyun Feng[a,b], Jiayue Zhang[a], Lu Bai[a], Guanshui Ma[a,*], Zhenyu Wang[a], Aiying Wang[a,b,*]

[a] State Key Laboratory of Advanced Marine Materials, Zhejiang Key Laboratory of Extreme-environmental Material Surfaces and Interfaces, Ningbo Institute of Materials Technology and Engineering, Chinese Academy of Sciences, Ningbo 315201, China
[b] Center of Materials Science and Optoelectronics Engineering, University of Chinese Academy of Sciences, Beijing 100049, China

ARTICLE INFO

Article history:
Received 9 June 2026
Revised 6 July 2026
Accepted 7 July 2026
Available online 20 July 2026

Keywords:
MAX phase coating
Solid solution
Corrosion resistance
Conductivity
Passivation film

ABSTRACT

Obtaining a laminated passivation film structure by regulating the selective oxidation sequence of elements is an effective method to enhance the corrosion resistance and conductivity of metal plates in proton exchange membrane fuel cells (PEMFCs). The study investigates the regulatory mechanism of the electrochemical corrosion behavior and microstructural evolution of $Ti_2(Al_{1-X}Sn_X)C$ coatings by different Sn solid solution contents. Comparative analysis reveals a non-monotonic dependence of corrosion resistance on Sn content. For the low-Sn coating ($X = 0.06$), the insufficient Sn content precludes the formation of a fully continuous SnO_2 capping layer, leaving the underlying Al_2O_3 vulnerable to dissolution by HF. The high-Sn coating ($X = 0.17$) suffers from severe lattice expansion and structural instability due to excessive Sn substitution. The oxidation potential difference among the three elements, Sn, Al, and Ti, is smoothed out by surface defects, causing them to oxidize almost simultaneously, forming a mixed rather than layered oxide with a disordered structure and poor protective properties. The optimal stoichiometry ($X = 0.09$) overcomes these limitations by forming a dense, defect-free $SnO_2/Al_2O_3/TiO_2$ composite passive film, achieving the lowest corrosion current density (4.07×10^{-7} A cm^{-2}) and minimal contact resistance degradation.

1. Introduction

With growing emphasis on clean energy technologies, proton exchange membrane fuel cells (PEMFCs) have emerged as ideal power sources owing to their high efficiency and environmental compatibility [1]. However, as a key component of the PEMFCs, metal bipolar plates account for approximately 80% of the weight and 40% of the cost [2]. Currently, several metals and metallic alloys such as aluminum, titanium, copper alloys, and nickel alloys are considered as possible bipolar plate materials. Among them, SS316L has become a leading candidate for commercial applications. Compared to highly conductive but easily corroded metals like Al and Cu, SS316L offers superior baseline corrosion resistance; compared to Ti and Ni, it presents a significant cost advantage. Furthermore, SS316L exhibits excellent machinability and can be easily fabricated into the required shape to accommodate complex flow channels in PEMFCs. In the weak acidic operating environment (60–80 °C, pH 2–3), bipolar plates are prone to dissolution and corrosion, leading to an increase in interfacial contact resistance (ICR), which in turn results in reduced output power and shortened service life [3]. Surface protection coating technologies such as noble metal coatings [4], metallic carbide coatings [5], conductive polymer composite coatings [6], amorphous carbon coatings [7], and $M_{n+1}AX_n$ (MAX) phase coatings [8] provide an effective solution to this problem. These coatings can significantly enhance the electrical conductivity and corrosion resistance of the bipolar plates while maintaining the properties of the substrate [9].

Ti_2AlC MAX phase exhibits exceptional electrical conductivity (reaching 4.42×10^6 Ω^{-1} m^{-1} at room temperature) and chemical stability [10–12], making it a promising candidate for PEMFC bipolar plates. However, under harsh operating conditions (0.5 mol L^{-1} H_2SO_4 + 5 mg L^{-1} HF, 80 °C), the native passive film tends to thicken over time, resulting in unacceptably high ICR [13]. To address this trade-off, this work employs Sn solid solution modification to tailor the surface passive film, aiming to decouple corrosion resistance from electrical conductivity.

In our previous study, we successfully established a "$SnO_2/Al_2O_3/TiO_2$" tri-layer composite passive film system by modifying the Ti_2AlC MAX phase with Sn solid solution [14]. As a

* Corresponding authors.
E-mail addresses: maguanshui@nimte.ac.cn (G. Ma), aywang@nimte.ac.cn (A. Wang).

https://doi.org/10.1016/j.jmst.2026.07.027
1005-0302/

modifying element, the solid solution content of Sn directly affects the crystal structure of the Ti_2AlC MAX phase, as well as the formation process and compositional ratio of the surface passive film. However, the precise mechanisms governing how Sn content (X-value in $Ti_2(Al_{1-X}Sn_X)C$) influences the coating's electrochemical behavior and electrical conductivity remain unclear [15,16]. Optimizing the Sn concentration is critical for balancing the formation of oxide constituents ($SnO_2/Al_2O_3/TiO_2$) in the passive layer, regulating elemental diffusion kinetics, and controlling defect formation energies. However, whether a continuously higher Sn content improves performance or introduces adverse structural degradation remains a critical unknown in current MAX phase research. Therefore, this study aims to determine the optimal solid-solution threshold. All these factors collectively determine the coating's long-term durability in PEMFC environments.

In this study, we systematically investigate the influence of Sn content on the microstructure, composition, and structure of the surface passivation film, corrosion kinetics, and electrical conductivity of Ti_2AlC MAX phases. It is showed the structure-property relationship is defined as "Sn content–passivation film structure–conductivity/corrosion resistance". The study further refines the modification theory of MAX phase materials, providing key technical parameters and scientific guidance for the development of high-performance PEMFC bipolar plate materials.

2. Experimental

2.1. Coating preparation

$Ti_2(Al_{1-X}Sn_X)C$ MAX phase coatings were synthesized on 316 L stainless steel (SS316L) substrates utilizing a hybrid deposition system. This system integrated high-power impulse magnetron sputtering (HiPIMS) and direct current magnetron sputtering (DCMS) sources within a PECVD-compatible, multi-target configuration, along with standard vacuum, gas delivery, and active cooling subsystems. The fundamental preparation process was based on our previous research [14]. The core procedure includes substrate pretreatment, argon ion etching, TiC transition layer deposition, Ti-Al-Sn-C layer co-sputtering, and vacuum annealing to crystallize into the MAX phase. Specifically, the samples were annealed at 750 °C for 90 min in a vacuum furnace ($< 3 \times 10^{-4}$ Pa) with a heating rate of 10 °C min^{-1}, followed by natural cooling.

Building upon the previously reported process, this experiment achieves the regulation of tin content in the coating primarily by adjusting the composition of the aluminum-tin alloy targets and optimizing the process parameters for each preparation step. The single aluminum-tin alloy target (Al:Sn = 90:10 at.%) used in the reported process was replaced with three targets of varying atomic ratios (Al:Sn = 95:5, 90:10, and 80:20 at.%) to realize a gradient regulation of Sn content in the $Ti_2(Al_{1-X}Sn_X)C$ MAX phase coatings. Additionally, the deposition temperature (100 °C) and substrate bias (−120 V) were optimized to promote the solid solution of Sn.

2.2. Characterization methods

The microstructure and chemical composition of the annealed coatings were characterized by scanning electron microscopy (SEM, FEI Quanta FEG 250) equipped with an energy-dispersive X-ray spectroscopy (EDS) detector. Phase identification was carried out by X-ray diffraction (XRD) on a Bruker D8 Advanced diffractometer with Cu K_α radiation (λ = 1.54056 Å). The chemical states of the elements were further analyzed by X-ray photoelectron spectroscopy (XPS). For detailed microstructural and chemical analysis, transmission electron microscopy (TEM) was performed on a Talos F200X field-emission microscope operated at 200 keV. This was complemented by high-resolution TEM (HRTEM), scanning TEM (STEM), and STEM-EDS mapping using a high-angle annular dark-field (HAADF) detector.

2.3. Electrochemical and ICR test

The corrosion resistance of the coatings was evaluated using a Gamry electrochemical workstation in a 0.5 mol L^{-1} H_2SO_4 solution containing 5 mg L^{-1} HF at 80 °C, with an exposed area of 1 cm^2. A standard three-electrode cell was employed, comprising the coating sample as the working electrode, a saturated Ag/AgCl reference electrode, and a platinum sheet counter electrode [17]. Potentiodynamic polarization was performed from −0.6 to 0.8 V (vs. Ag/AgCl) at a scan rate of 0.5 mV s^{-1}. To assess the long-term stability, a potentiostatic test was conducted by holding the potential at 0.6 V (vs. Ag/AgCl) for 24 h [18].

The ICR was measured using a two-probe method with carbon paper (Toray TGP-H-60) as the intermediate conductive layer. The sample was sandwiched between two pieces of carbon paper, which were then placed between two gold-plated copper plates. A computer-controlled mechanical testing machine (CMT5150) applied a controlled compaction pressure of 1.5 MPa to the assembly. This specific pressure was selected to simulate typical stack clamping forces (1.0–2.0 MPa) in practical PEMFCs, whilst slightly exceeding the Department of Energy (DOE) benchmark pressure of 1.4 MPa. The resistance was measured using a low DC resistance tester (JK2511B). The ICR value was derived by subtracting the intrinsic resistance of the carbon paper, which was characterized separately under identical pressures. Each sample was tested at least five times to ensure statistical reliability.

3. Results and discussion

3.1. Composition and microstructure characteristics

Fig. 1 presents the surface morphologies of the synthesized $Ti_2(Al_{1-X}Sn_X)C$ MAX phase coatings with different Sn contents. All coatings display uniform and compact microstructures, showing no visible defects such as cracks or pores. The EDS confirmed that the Ti: (Al + Sn): C atomic ratios for all three coatings were close to the characteristic 2:1:1 stoichiometry of MAX phases. According to the measured Sn contents (1.93, 3.37, and 5.65 at.%), the coatings are denoted as $Ti_2(Al_{0.94}Sn_{0.06})C$, $Ti_2(Al_{0.91}Sn_{0.09})C$, and $Ti_2(Al_{0.83}Sn_{0.17})C$. For simplicity, these are referred to hereafter by their Sn molar fractions as X = 0.06, 0.09, and 0.17, respectively.

Fig. 2 shows the XRD patterns of $Ti_2(Al_{1-X}Sn_X)C$ solid-solution MAX phase coatings with varying Sn contents (X = 0.06, 0.09, and 0.17). All coatings display distinct diffraction peaks corresponding to a high-purity MAX phase, consistent with the reference pattern (PDF#29–0025) [19]. The MAX phase peaks are notably more intense than those from the substrate. As illustrated in Fig. 2(b), within the 2θ range of 38°–44°, the substrate peak positions remain nearly identical for all compositions. In contrast, the MAX phase diffraction peaks systematically shift to lower angles with increasing Sn content. Incorporating larger atomic radius Sn into the crystal structure expands the lattice parameters of the MAX phase [20,21], leading to the observed peak displacement. As reported in a previous study [22], the substitution of Al by larger Sn atoms inevitably induces structural strain and distorts the M_6A trigonal prisms within the nanolaminated structure. This inherent lattice distortion, while initially accommodating the solid solution, destabilizes the phase thermodynamically when the Sn content exceeds an optimal threshold [23]. These findings demonstrate successful substitution of Al by Sn at the A-site, confirming the formation of a $Ti_2(Al_{1-X}Sn_X)C$ solid solution with tunable Sn composition.

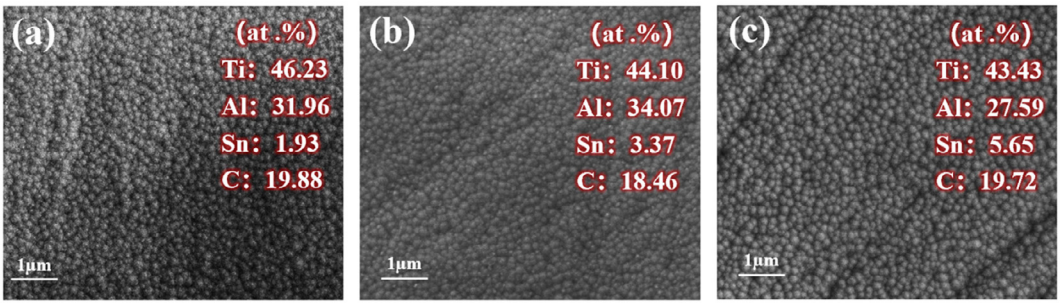

Fig. 1. SEM images and EDS compositional results of the $Ti_2(Al_{1-X}Sn_X)C$ coatings: (a) $Ti_2(Al_{0.94}Sn_{0.06})C$, (b) $Ti_2(Al_{0.91}Sn_{0.09})C$, and (c) $Ti_2(Al_{0.83}Sn_{0.17})C$.

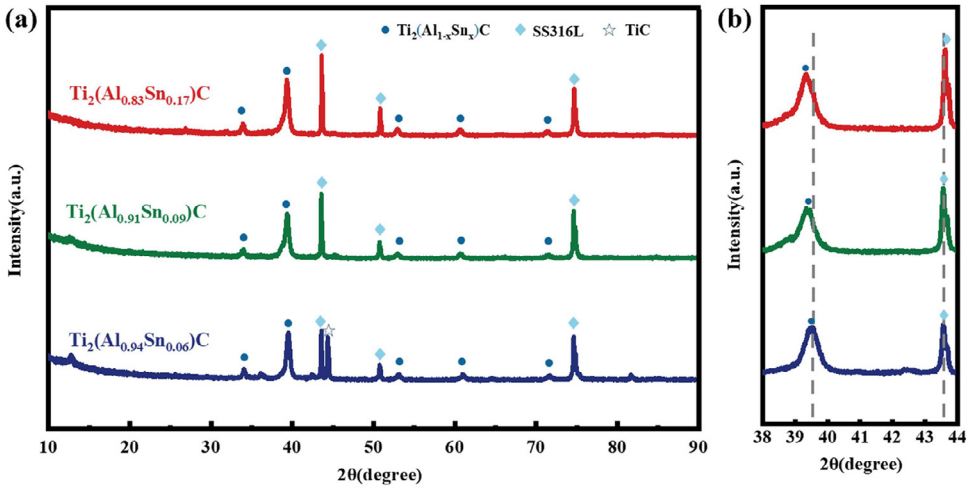

Fig. 2. (a) XRD patterns of $Ti_2(Al_{1-X}Sn_X)C$ MAX phase coatings (X = 0.06, 0.09, and 0.17), and (b) local enlarged images over the 2θ range of 38°–44°.

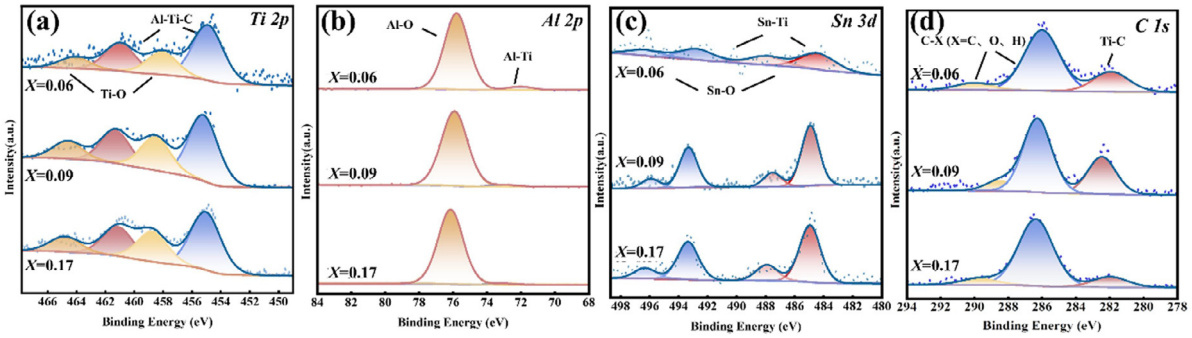

Fig. 3. XPS spectra of $Ti_2(Al_{1-X}Sn_X)C$ MAX phase coatings (X = 0.06, 0.09, and 0.17): (a) Ti 2p, (b) Al 2p, (c) Sn 3d, and (d) C 1s.

The chemical bonding states of the coatings were investigated by XPS. The high-resolution spectra of the Ti 2p, Al 2p, Sn 3d, and C 1s core levels are presented in Fig. 3. To eliminate surface contamination, all samples were subjected to 5 min of Ar^+ ion sputtering prior to measurement. As shown in Fig. 3(a), the Ti 2p spectra exhibit no significant differences among the three coatings. Each spectrum was deconvoluted into four peaks. The doublets at binding energies of 454.8/460.9 eV (X = 0.06), 455.1/461.2 eV (X = 0.09), and 455.0/461.1 eV (X = 0.17) are assigned to Ti $2p_{3/2}$ and Ti $2p_{1/2}$, respectively [14,17]. The remaining doublets at 458.1/464.2 eV (X = 0.06), 458.5/464.6 eV (X = 0.09), and 458.7/464.8 eV (X = 0.17) are associated with Ti–O bonds, indicating the presence of a minor surface oxide that persisted even after sputtering.

The Al 2p spectra of all three coatings exhibit two characteristic peaks (Fig. 3(b)). The peaks located at binding energies of 72.1 eV (X = 0.06), 72.9 eV (X = 0.09), and 73.0 eV (X = 0.17) are attributed to Al–Ti bonds, while those at 75.7 eV (X = 0.06), 75.9 eV (X = 0.09), and 76.1 eV (X = 0.17) correspond to Al–O bonds [23]. The much higher intensity of the Al–O bonds compared to the Al–Ti bonds indicates partial oxidation of the coatings during the annealing process. Furthermore, with increasing Sn content, the dissolution of Sn atoms and their bonding with other elements lead to a gradual weakening of the Al–Ti bond strength, a trend that is clearly observable in Fig. 3(b). Specifically, for the X = 0.17 coating, the Al–Ti signal becomes almost negligible. Notably, the Al 2p peaks exhibit a systematic positive shift toward higher binding energies with increasing Sn content. This shift reflects a localized reduction in electron density around the Al atoms, driven by the higher electronegativity of the substituting Sn atoms (1.96 vs. 1.61 for Al).

The Sn 3d spectra of the three coatings each exhibit four fitted peaks. The peaks at 484.5 and 492.9 eV (X = 0.06), 484.9 and 493.3 eV (X = 0.09), and 485.0 and 493.3 eV (X = 0.17) are as-

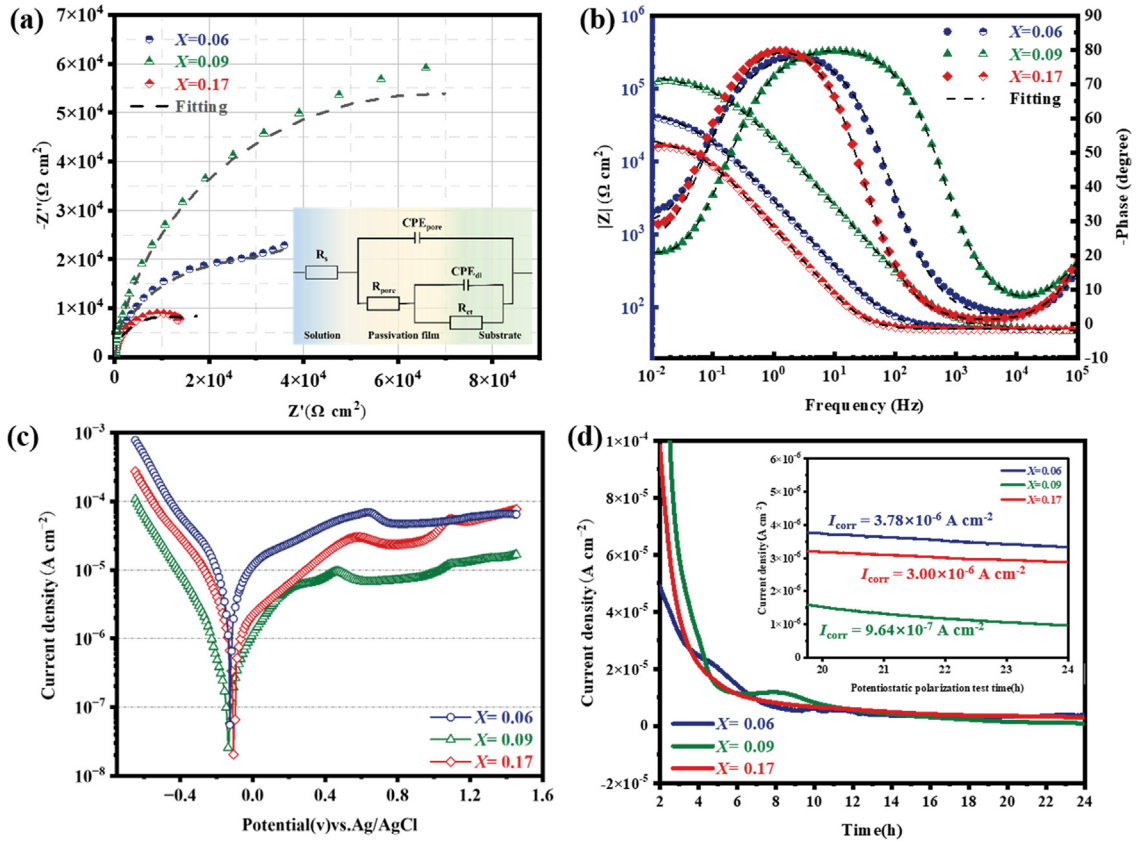

Fig. 4. EIS of $Ti_2(Al_{1-X}Sn_X)C$ MAX phase coatings (X = 0.06, 0.09, and 0.17) in 0.5 mol L^{-1} H_2SO_4 + 5 mg L^{-1} HF, 80 °C: (a) Nyquist plots, (b) Bode plots. The inset in (a) is the equivalent electrical circuit used to fit the impedance spectra. (c) Potentiodynamic polarization curves of $Ti_2(Al_{1-X}Sn_X)C$ MAX phase coatings (X = 0.06, 0.09, and 0.17) in 0.5 mol L^{-1} H_2SO_4 + 5 mg L^{-1} HF, 80 °C and (d) potentiostatic test curves for 24 h with an inset showing a magnified view of the period from 20 to 24 h.

signed to the $3d_{5/2}$ and Sn $3d_{3/2}$ spin–orbit components, respectively [24,25]. The remaining peaks correspond to Sn–O bonds. For X = 0.06, the Sn content in the coating is relatively low, resulting in weaker binding intensity. As the Sn content increases, the binding intensity gradually strengthens.

The C 1s spectra of the three coatings were each fitted with three component peaks. The peaks located at binding energies of 281.9 eV (X = 0.06), 282.4 eV (X = 0.09), and 282.1 eV (X = 0.17) are assigned to the Ti–C bond [17]. The remaining spectral features are likely attributable to surface oxidation during heat treatment and the adsorption of adventitious carbon contaminants from ambient air. Due to the high electrical conductivity and unique chemical environment of MAX phases, using the standard C 1s peak (284.8 eV) for calibration would lead to inaccurate binding energies.

3.2. Electrochemical measurements

Electrochemical impedance spectroscopy (EIS) measurements were conducted on $Ti_2(Al_{1-X}Sn_X)C$ solid-solution MAX phase coatings (X = 0.06, 0.09, and 0.17) under PEMFCs accelerated testing operating conditions (0.5 mol L^{-1} H_2SO_4 + 5 mg L^{-1} HF, 80 °C). The corresponding electrochemical impedance spectra are presented in Fig. 4. As depicted in the Nyquist plot (Fig. 4(a)), all three coatings exhibit incomplete capacitive arcs over the entire frequency range. The diameter of the capacitive arc reflects the impedance of the passive film and the charge transfer resistance. Generally, a larger arc diameter indicates higher passive film impedance, greater difficulty in charge transfer, and consequently, improved corrosion resistance. The capacitive arc diameters decrease in the order: X = 0.09, X = 0.06, X = 0.17. This trend suggests that the $Ti_2(Al_{0.91}Sn_{0.09})C$ coating (X = 0.09) possesses the best electrochemical corrosion resistance in this environment, followed by $Ti_2(Al_{0.94}Sn_{0.06})C$ (X = 0.06), with $Ti_2(Al_{0.83}Sn_{0.17})C$ (X = 0.17) exhibiting the lowest performance. Furthermore, the Bode plot (Fig. 4(b)) reveals that the $Ti_2(Al_{0.91}Sn_{0.09})C$ coating maintains a higher and more stable phase angle over a broader frequency range (10^{-2} to 10^2 Hz).

The EIS data were analyzed by fitting to an equivalent circuit model (Fig. 4(a) inset) to further investigate the behavior of the three coatings in 0.5 mol L^{-1} H_2SO_4 + 5 mg L^{-1} HF at 80 °C. The circuit includes the solution resistance (R_s), the passive film resistance (R_1), and the charge transfer resistance (R_{ct}) [26,27]. To account for surface heterogeneity and roughness, a constant phase element (CPE) was adopted in place of an ideal capacitor (C). CPE_1 corresponds to the coating capacitance, and CPE_2 represents the double-layer capacitance at the substrate/electrolyte interface [28–30]. The impedance of a CPE could be given by:

$$Z_{CPE} = \left[Q(j\omega)^n\right]^{-1} \quad (1)$$

where $j = -1^{0.5}$ is the imaginary number, $\omega = 2\pi f$ is the angular frequency, Q is the frequency-independent CPE parameter, and n is an exponential factor ($0 \le n \le 1$). When n = 1, the CPE behaves as an ideal capacitor. The fitting results are summarized in Table 1. The quality of the fit was confirmed by chi-squared (χ^2) values on the order of 10^{-4}, indicating that the model accurately represents the electrochemical corrosion behavior under the tested conditions [31,32]. Crucially, R_{ct} serves as a key indicator of corrosion resistance [33].

As shown in Table 1, the coating with X = 0.09 exhibits a significantly higher R_{ct} (3.37×10^5 Ω cm^2) compared to X = 0.06

Table 1
Fitting results of EIS spectra for $Ti_2(Al_{1-X}Sn_X)C$ MAX phase coatings (X = 0.06, 0.09, and 0.17) in 0.5 mol L^{-1} H_2SO_4 + 5 mg L^{-1} HF, 80 °C.

Sample	R (Ω cm^2)	CPE_1		R_1 (Ω cm^2)	CPE_2		R_{ct} (Ω cm^2)	W (Ω $s^{0.5}$ cm^2)	χ^2 (10^{-4})
		Q_1 (F cm^{-2})	n		Q_2 (F cm^{-2})	n			
X = 0.06	1.69 × 10^{-4}	7.28 × 10^{-7}	0.85	51.31	6.40 × 10^{-5}	0.91	3.29 × 10^4	1.71 × 10^{-4}	10.76
X = 0.09	0.002	6.56 × 10^{-9}	0.99	83.81	1.99 × 10^{-4}	0.94	3.37 × 10^5	6.86 × 10^{-4}	1.68
X = 0.17	0.001	7.28 × 10^{-7}	1.00	49.81	1.40 × 10^{-4}	0.95	1.46 × 10^4	5.07 × 10^{-4}	2.05

Table 2
Electrochemical parameters extracted from potentiodynamic polarization curves of $Ti_2(Al_{1-X}Sn_X)C$ MAX phase coatings (X = 0.06, 0.09, and 0.17) in 0.5 mol L^{-1} H_2SO_4 + 5 mg L^{-1} HF, 80 °C.

Sample	E_{corr} (V)	I_{corr} (A cm^{-2})	β_a (mV dec^{-1})	β_c (mV dec^{-1})
X = 0.06	−0.11	1.80 × 10^{-6}	534.10	243.80
X = 0.09	−0.13	4.07 × 10^{-7}	278.40	202.70
X = 0.17	−0.24	1.12 × 10^{-5}	907.60	327.40

(3.29 × 10^4 Ω cm^2) and X = 0.17 (1.46 × 10^4 Ω cm^2). This order-of-magnitude increase in R_{ct} confirms that the optimized Sn content (X = 0.09) effectively hinders the charge transfer process at the electrolyte/electrode interface. A higher R_1 value generally indicates a more compact and highly resistive passive film, which enhances barrier properties. As shown in Table 1, the coating with X = 0.09 ($Ti_2(Al_{0.91}Sn_{0.09})C$ exhibits a markedly larger R_1 than the other compositions, suggesting it offers the best corrosion protection. In contrast, the inferior performance of X = 0.06 and X = 0.17 implies that deviations from the optimal stoichiometry may lead to microstructural defects or phase impurities, weakening the barrier properties against corrosive electrolyte penetration.

Fig. 4(c) presents the potentiodynamic polarization curves of the three coatings in a 0.5 mol L^{-1} H_2SO_4 + 5 mg L^{-1} HF solution at 80 °C. The corresponding parameters obtained by Tafel extrapolation are summarized in Table 2. For all samples, the absolute value of the anodic Tafel slope (β_a) is greater than that of the cathodic Tafel slope (β_c), indicating that the corrosion process is anodically controlled [34]. In the anodic region, all coatings exhibit clear passivation behavior. The corrosion current density (I_{corr}) serves as a key kinetic parameter for evaluating corrosion rate, with lower values generally corresponding to better corrosion resistance. According to the fitting results, the $Ti_2(Al_{0.91}Sn_{0.09})C$ coating (X = 0.09) exhibits an I_{corr} of 4.07 × 10^{-7} A cm^{-2}, which is approximately one to two orders of magnitude lower than those of $Ti_2(Al_{0.94}Sn_{0.06})C$ (X = 0.06, I_{corr} = 1.80 × 10^{-6} A cm^{-2}) and $Ti_2(Al_{0.83}Sn_{0.17})C$ (X = 0.17, I_{corr} = 1.12 × 10^{-5} A cm^{-2}), indicating its superior corrosion resistance.

Fig. 4(d) displays the potentiostatic polarization curves of the three coatings after 24 h of testing in 0.5 mol L^{-1} H_2SO_4 + 5 mg L^{-1} HF at 80 °C, evaluating their long-term service stability. The current density of all samples decreased continuously over time and eventually stabilized, indicating a gradual reduction in corrosion rate that was maintained at a low level. The steady-state I_{corr} were 3.78 × 10^{-6} A cm^{-2} ($Ti_2(Al_{0.94}Sn_{0.06})C$), 9.64 × 10^{-7} A cm^{-2} ($Ti_2(Al_{0.91}Sn_{0.09})C$), and 3.00 × 10^{-6} A cm^{-2} ($Ti_2(Al_{0.83}Sn_{0.17})C$), respectively. These results are consistent with those obtained from the potentiodynamic polarization tests, further confirming that the $Ti_2(Al_{0.91}Sn_{0.09})C$ coating exhibits the best corrosion resistance. Therefore, in terms of corrosion current density, this coating provides the strongest protection to the substrate, whereas either too low or too high Sn solid-solution content leads to degraded protective performance.

Fig. 5 presents the variation in ICR of three $Ti_2(Al_{1-X}Sn_X)C$ solid-solution MAX phase coatings (X = 0.06, 0.09, and 0.17) before and after 24 h of potentiostatic polarization testing. After prolonged polarization, the ICR values of all samples increased. For the $Ti_2(Al_{0.91}Sn_{0.09})C$ coating, the sample exhibited the least variation, with ICR values of 9.10 mΩ cm^2 before and 9.40 mΩ cm^2 after corrosion. In contrast, for the $Ti_2(Al_{0.94}Sn_{0.06})C$ coating, the ICR increased markedly from 13.00 to 18.60 mΩ cm^2, while for the $Ti_2(Al_{0.83}Sn_{0.17})C$ coating, it rose from 8.10 to 10.32 mΩ cm^2. This behavior can be attributed to the influence of Sn solid-solution content on the coating structure and electrical conductivity. At a lower Sn content (X = 0.06), conductive SnO_2 oxide layers may not form sufficiently, thereby compromising conductivity. Conversely, excessive Sn content (X = 0.17) may lead to a more porous coating structure, resulting in noticeable degradation during corrosion.

3.3. Passive film characteristics

To elucidate the microstructural evolution of passive films formed on the three coatings, cross-sectional specimens were prepared by focused ion beam (FIB) milling from specimens after 24 h of potentiostatic polarization.

Fig. 6(a, b) shows cross-sectional STEM-HAADF images and corresponding EDS elemental maps of the $Ti_2(Al_{0.94}Sn_{0.06})C$ coating after potentiostatic polarization. Fig. 6(a) reveals pronounced O and Al enrichment at Position ③ (O = 67.98 at.% and Al = 24.65 at.%; Table 3), indicating the formation of an Al-bearing oxide layer (predominantly Al_2O_3), albeit with an apparent O excess attributable to TEM foil geometry and/or surface hydroxylation/adsorption. Coexistence of Ti-enriched domains (Position ①) immediately adjacent to Al/O-enriched domains (Position ②) suggests Ti–Al microsegregation during oxidation. Fig. 6(b) presents a bright-field (BF) image of the same region, with an inset HRTEM image (white box). The coating comprises an amorphous matrix, nanocrystalline particles, and minor lath-like MAX phases. Fourier transform analysis of localized grains measured an interplanar spacing of 0.44 nm, matching the (111) plane of Al_2O_3, confirming Al_2O_3 as the main oxide phase formed in the coating.

Fig. 7(a) presents the cross-sectional STEM-HAADF image and EDS elemental maps of the $Ti_2(Al_{0.91}Sn_{0.09})C$ coating after 24 h of potentiostatic polarization. The elemental maps reveal pronounced partitioning of Sn, Al, and Ti within the passive film, leading to a stratified oxide architecture. From the surface inward, three sublayers can be identified: an outer Sn-rich layer (Position ③: 8.47 at.% Sn), an intermediate Al-rich layer (Position ②: 24.53 at.% Al), and an inner Ti-rich layer (Position ①: 30.7 at.% Ti) (Fig. 7(a) and Table 4). Table 4 summarizes the elemental composition of Positions ①, ②, and ③ in the STEM-HAADF images presented in Fig. 7, with atomic percentages directly indicating the chemical characteristics of each layer. Fig. 7(b) shows the corresponding cross-sectional TEM morphology and selected-area electron diffraction (SAED) patterns from these regions. Diffraction analysis indicates that both Position ① (Ti-rich) and Position ② (Al-

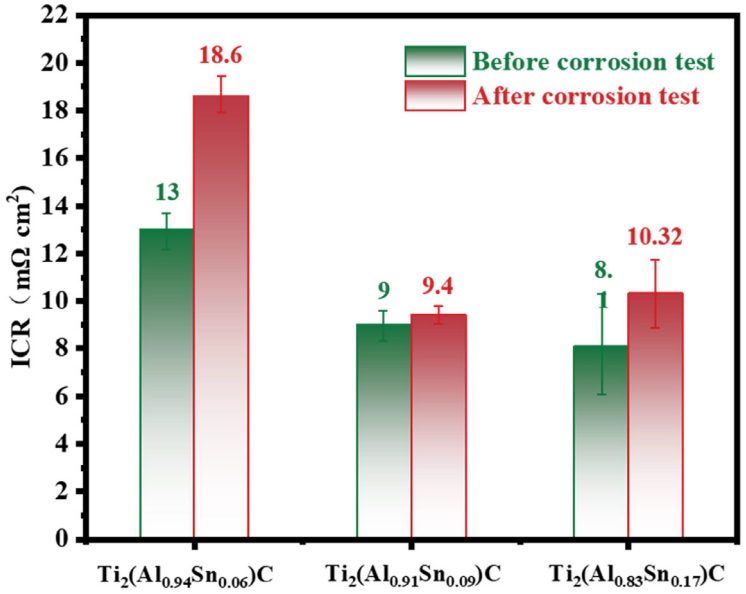

Fig. 5. The ICR values of $Ti_2(Al_{1-X}Sn_X)C$ MAX phase coatings (X = 0.06, 0.09, and 0.17) before and after 24 h potentiostatic tests in 0.5 mol L^{-1} H_2SO_4 + 5 mg L^{-1} HF, 80 °C.

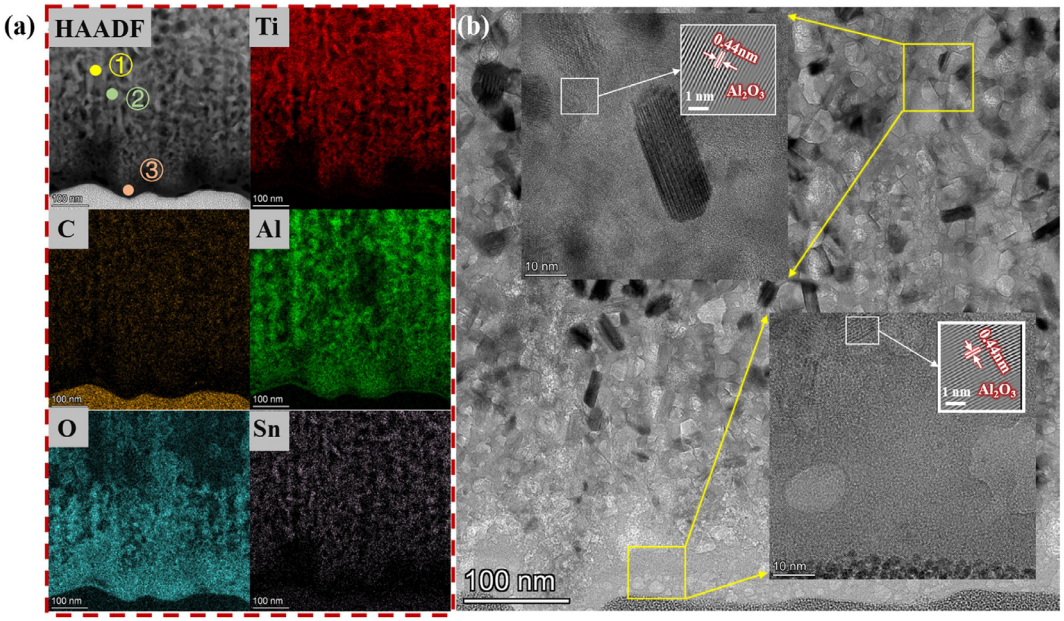

Fig. 6. (a) STEM-HAADF image and EDS elemental maps of the $Ti_2(Al_{0.94}Sn_{0.06})C$ coating after 24 h potentiostatic polarization in 0.5 mol L^{-1} H_2SO_4 + 5 mg L^{-1} HF at 80 °C; (b) bright-field TEM image of the same region, with an HRTEM inset and the corresponding Fourier filtered image of the selected area.

Table 3
The elemental content of the selected location in the STEM-HAADF image in Fig. 6 (at.%).

	Ti	Al	C	Sn	O
Position ①	48.55	22.03	4.98	16.23	8.21
Position ②	9.30	33.46	0.79	6.97	49.48
Position ③	3.27	24.65	0.28	3.81	67.98

Table 4
The elemental content of the selected location in the STEM-HAADF image in Fig. 7 (at.%).

	Ti	Al	C	Sn	O
Position ①	30.7	0.42	2.33	5.49	61.06
Position ②	24.26	24.53	2.01	8.16	41.05
Position ③	19.19	1.33	8.47	5.52	65.49

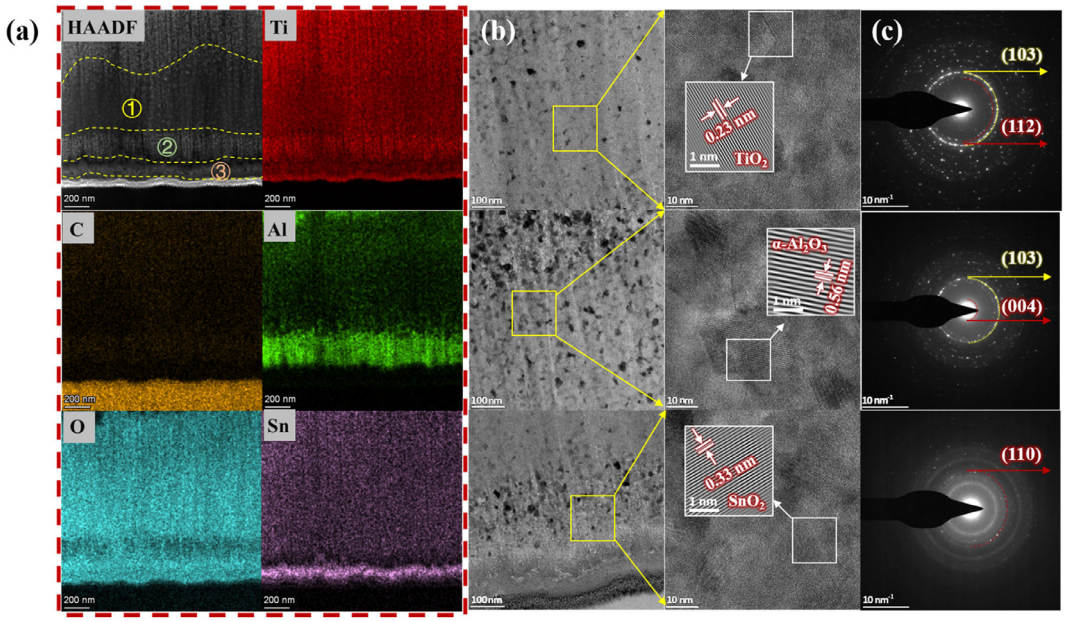

Fig. 7. (a) STEM-HAADF image and EDS elemental maps of the $Ti_2(Al_{0.91}Sn_{0.09})C$ coating after 24 h potentiostatic polarization in 0.5 mol L^{-1} H_2SO_4 + 5 mg L^{-1} HF at 80 °C; (b) bright-field TEM images of the boxed region in (a) with HRTEM/FFT insets for position of ①–③; (c) SAED patterns corresponding to position of ①–③ (rings indexed in the figure).

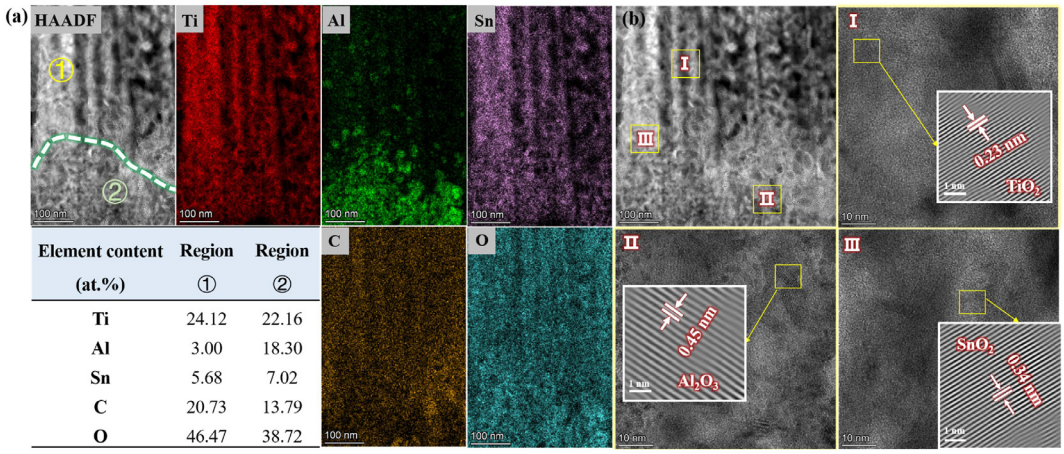

Element content (at.%)	Region ①	Region ②
Ti	24.12	22.16
Al	3.00	18.30
Sn	5.68	7.02
C	20.73	13.79
O	46.47	38.72

Fig. 8. (a) STEM-HAADF image and EDS elemental maps of the $Ti_2(Al_{0.83}Sn_{0.17})C$ coating after 24 h potentiostatic polarization in 0.5 mol L^{-1} H_2SO_4 + 5 mg L^{-1} HF at 80 °C; (b) bright-field TEM image of the same region, with an HRTEM inset and the corresponding Fourier-filtered image of the selected area.

rich) exhibit polycrystalline diffraction rings. Fourier transform of the SAED pattern from Position ① reveals interplanar spacings of 0.21 and 0.59 nm in the white-marked zone, corresponding to the (112) plane of TiO_2 and the (004) plane of Al_2O_3, respectively. In contrast, the SAED pattern of Position ③ displays diffuse rings characteristic of an amorphous phase, superimposed with nanocrystalline diffraction rings. Fourier analysis of the marked region identifies a spacing of 0.35 nm, matching the (110) plane of SnO_2, which confirms that SnO_2 is the primary constituent of this layer.

Fig. 8 presents the STEM-HAADF images and corresponding elemental maps of the $Ti_2(Al_{0.83}Sn_{0.17})C$ coating, with Fig. 8(a) revealing complete oxidation characterized by a uniformly distributed oxygen signal throughout the coating, indicating a significantly accelerated corrosion process.

The elemental distribution of Ti and Al reveals two distinct regions within the oxidized structure: a Ti-rich zone (Region ①) and an Al-rich zone (Region ②). EDS analysis further clarifies the phase characteristics of these regions. The atomic Ti/O ratio close to 1:2 in Region ① is consistent with TiO_2 as the primary phase, while the markedly increased and dominant Al content in Region ② indicates the predominant formation of Al_2O_3. Fig. 8(b) presents a bright-field image of the red-boxed area, with an inset showing an HRTEM image acquired from the white-boxed region. The oxide layer consists of an amorphous matrix embedded with nanocrystalline particles. Fast Fourier transform (FFT) analysis of distinct lattice fringes reveals interplanar spacings of 0.23, 0.45, and 0.34 nm corresponding to the (112) plane of TiO_2, the (111) plane of Al_2O_3, and the (110) plane of SnO_2, respectively. These results confirm that the oxide layer formed during passivation comprises TiO_2, Al_2O_3, and SnO_2. Unlike the well-stratified and protective passive film observed in the $X = 0.09$ coating, the $X = 0.17$ coating undergoes severe and complete oxidation. This accelerated degradation is fundamentally driven by the severe lattice distortion and structural instability identified in the XRD analysis. Recent first-principles calculations and oxidation studies have demonstrated that excessive Sn substitution significantly weakens the Ti-Al (M-A) atomic bonds within the MAX phase lattice [35,36].

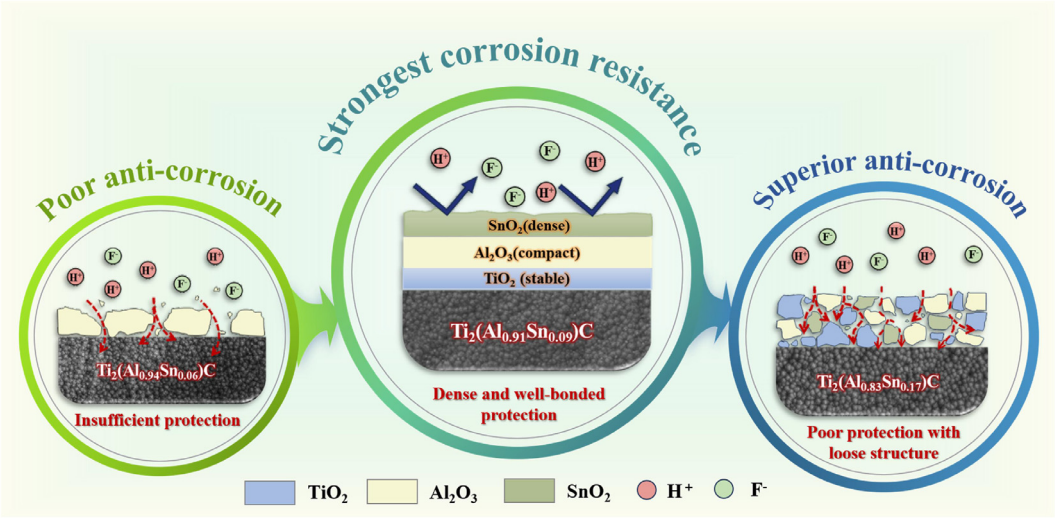

Fig. 9. Schematic diagram showing the passivation mechanism and process of $Ti_2(Al_{1-X}Sn_X)C$ MAX phase coatings (X = 0.06, 0.09, and 0.17) in 0.5 mol L^{-1} H_2SO_4 + 5 mg L^{-1} HF, 80 °C.

This weakened interlayer bonding lowers the activation energy required for the inward diffusion of corrosive species (e.g., O^{2-} and F^-). Consequently, rather than forming a dense, continuous SnO_2 capping layer, the destabilized structure is rapidly infiltrated by the electrolyte, leading to the global, non-protective oxidation observed in Fig. 8.

Through systematic experimental investigations and multi-scale characterization, this study reveals the regulatory mechanism of Sn content (X) on the structural characteristics and electrochemical corrosion resistance of $Ti_2(Al_{1-X}Sn_X)C$ solid-solution MAX phase coatings. As illustrated in Fig. 9, the mechanism is closely linked to the stability of the passive film in the fluoride-containing acidic environment. We suggest that in Ti_2AlC with low Sn content, Al is the A-site element and exhibits the highest chemical activity. In acidic solutions containing F^-, Al undergoes preferential selective dissolution [37,38]. However, under constant potential polarization, the dissolved Al^{3+} rapidly hydrolyzes and deposits, forming a single, relatively loose Al_2O_3 film. We speculate that Al_2O_3 is thermodynamically unstable in acidic environments containing F^- (tends to form AlF_6^{3-} complexes), leading to the presence of micropores or local dissolution in the film, which results in limited barrier properties [22]. Therefore, the corrosion resistance of the X = 0.06 sample is poor.

For the $Ti_2(Al_{0.91}Sn_{0.09})C$ coating, the outer SnO_2 layer, due to the standard electrode potential of Sn (Sn^{2+}/Sn, −0.14 V vs. SHE), is higher than that of Al (−1.66 V). During the initial stage of polarization, the surface-enriched Sn will preferentially precipitate as SnO_2. SnO_2 exhibits extremely high chemical stability in F^- containing acidic solutions, forming a dense outer protective shield that blocks the inward diffusion of F^- and H_2O. After the formation of the outer SnO_2 layer, the interface pH value is reduced and F^- is blocked. This allows Al^{3+} to undergo uniform and slow hydrolysis within the confined space, depositing to form a dense, amorphous Al_2O_3 intermediate layer. The Ti element has a lower potential (Ti^{4+}/Ti, −0.86 V), but due to its combination with C to form M–X bonds in the MAX phase, its dissolution kinetics are relatively slow. After the formation of the outer two layers, the interface environment has stabilized (pH increases, F^- decreases), and a small amount of dissolved Ti^{4+} hydrolyzes at the alloy/film interface, forming an extremely thin TiO_2 layer with high lattice matching to the substrate. As an n-type semiconductor, TiO_2 has an internal electric field that helps to block ion migration. The layered structure significantly increases the tortuosity of ion/electron transport, making it extremely difficult for corrosive media to penetrate, thereby enhancing corrosion resistance.

For the high-Sn coating ($Ti_2(Al_{0.83}Sn_{0.17})C$), the oversized substitution of Al by large-sized Sn atoms introduces a substantial number of defects on the surface, such as dislocations and vacancies, as evidenced by the preceding XRD analysis. These defects act as fast diffusion channels, transitioning the dissolution reaction from a uniform mode to a localized pitting initiation mode. Under high Sn content, the differences in oxidation potentials among Sn, Al, and Ti are smoothed out by these surface defects, causing them to undergo oxidation almost simultaneously and form a mixed rather than a layered oxide. Consequently, despite the overall higher oxide content, the disordered structure leads to poor protectiveness.

In all, it is not necessarily true that a higher solid solution content of Sn is better. Instead, there exists a “critical concentration for layered film formation”. An appropriate amount of solid solution of Sn alters the surface chemical activity of the A-site element (Al) in Ti_2AlC, inducing a transition from a “single layer” to a “functional gradient multilayer film” of the passivation layer. This achieves a balance between the synergistic blocking of electron/ion transport and chemical stability, thereby enhancing corrosion resistance.

4. Conclusion

In summary, an appropriate Sn content (X = 0.09) is critical for enhancing the protective effect by promoting the formation of a dense, uniform $SnO_2/Al_2O_3/TiO_2$ composite passive film. Deviation from this optimal stoichiometry leads to severe performance degradation. Specifically, a higher Sn concentration is not expected to be beneficial; while insufficient Sn results in chemical instability against acid/HF attack, excessive Sn (X = 0.17) induces severe lattice distortion and weakens M-A bonds. This instability disrupts the selective oxidation sequence, forming a non-protective mixed oxide rather than a dense barrier layer. Therefore, the Sn content (X) is the core factor regulating the coating’s corrosion resistance. To achieve excellent protective performance of $Ti_2(Al_{1-X}Sn_X)C$ coatings, precise control of Sn content is required to avoid performance degradation caused by insufficient or excessive Sn. From an industrial perspective, the optimal Sn modification intelligently regulates the selective oxidation sequence to form a gradient passive film, ensuring exceptional long-term ICR stability. Ultimately, this tailored strategy provides a scalable and cost-

effective pathway for deploying SS316L bipolar plates in commercial PEMFC systems.

CRediT authorship contribution statement

Jingyun Feng: Writing – original draft, Visualization, Validation, Conceptualization. **Jiayue Zhang:** Investigation, Formal analysis, Data curation. **Lu Bai:** Investigation, Conceptualization. **Guanshui Ma:** Writing – review & editing, Visualization, Project administration, Funding acquisition. **Zhenyu Wang:** Methodology, Investigation. **Aiying Wang:** Writing – review & editing, Visualization, Resources, Project administration, Funding acquisition, Conceptualization.

Declaration of competing interest

The authors declare that they have no known competing financial interests or personal relationships that could have appeared to influence the work reported in this paper.

Acknowledgments

This work was financially supported by the National Key R&D Program of China (2024YFB3816500), the National Natural Science Foundation of China (52571117), the Leading Innovative and Entrepreneur Team Introduction Program of Zhejiang (2024R01004), and the Zhejiang Provincial Natural Science Foundation of China (LD24E010003). Guanshui Ma gratefully acknowledges the support from the Open Research Fund of the State Key Laboratory of Tropic Ocean Engineering Materials and Materials Evaluation (STOEM2025KF003).

References

[1] G. Ma, A. Zhang, Z. Wang, K. Wang, J. Zhang, K. Xu, Y. Xu, S. Zhou, A. Wang, Mater. Horiz. 12 (2025) 1689–1710.
[2] G. Ma, H. Wu, Z. Fang, X. Zhou, R. Chen, W. Yang, J. Zhang, Z. Wang, A. Wang, J. Mater. Sci. Technol. 206 (2025) 176–184.
[3] Y. Xu, G. Ma, Z. Li, Y. Zhang, A. Zhang, Z. Wang, A. Wang, Corros. Sci. 257 (2025) 113351.
[4] G. Ma, J. Yan, N. Lin, P. Guo, W. Yang, C. Chen, A. Wang, Corros. Commun. 20 (2025) 33–41.
[5] G. Ma, Y. Zheng, J. Zhang, J. Yan, P. Guo, W. Yang, R. Chen, J. Yuan, L. Cui, J. Alloy. Compd. 933 (2023) 167855.
[6] H. Li, P. Guo, K. Komatsu, G. Ma, R. Chen, P. Ke, H. Saito, A. Wang, Int. J. Hydrogen Energy 91 (2024) 765–774.
[7] G. Ma, P. Guo, S. Wang, Y. Liu, Y. Xin, H. Li, R. Chen, A. Wang, Appl. Surf. Sci. 561 (2021) 149972.
[8] H. Liu, B. Wang, D. Li, B. Dong, J. Liu, P. Chen, Y. Bian, Q. Xu, Y. Fan, X. He, Eng. Fail. Anal. 186 (2026) 110577.
[9] Y. Zhang, S. Zhang, A. Zhang, G. Ma, K. Wang, Z. Wang, A. Wang, J. Adv. Ceram. 13 (2024) 1748–1758.
[10] H. Li, Y. Xin, K. Komatsu, P. Guo, G. Ma, P. Ke, K.-R. Lee, H. Saito, A. Wang, Int. J. Hydrogen Energy 47 (2022) 11622–11632.
[11] K. Wang, Z. Li, Y. Zhang, G. Ma, G. Zhou, P. Ke, Z. Wang, A. Wang, Surf. Interfaces 51 (2024) 104678.
[12] H. Li, P. Guo, D. Zhang, L. Liu, Z. Wang, G. Ma, Y. Xin, P. Ke, H. Saito, A. Wang, J. Power Sources 469 (2020) 228269.
[13] H. Liu, D. Li, P. Chen, W. Wang, H. Yang, R. Geng, H. Liu, Tribol. Int. 215 (2026) 111428.
[14] J. Zhang, Y. Zhang, Z. Wang, G. Ma, A. Zhang, K.-R. Lee, A. Wang, Corros. Sci. 255 (2025) 113073.
[15] W. Eom, H. Shin, W. Jeong, R.B. Ambade, H. Lee, T.H. Han, Mater. Horiz. 10 (2023) 4892–4902.
[16] W.-T. Cao, W. Feng, Y.-Y. Jiang, C. Ma, Z.-F. Zhou, M.-G. Ma, Y. Chen, F. Chen, Mater. Horiz. 6 (2019) 1057–1065.
[17] P.P. Michałowski, M. Anayee, T.S. Mathis, S. Kozdra, A. Wójcik, K. Hantanasirisakul, I. Jóźwik, A. Piątkowska, M. Możdżonek, A. Malinowska, R. Diduszko, E. Wierzbicka, Y. Gogotsi, Nat. Nanotechnol. 17 (2022) 1192–1197.
[18] S. Zhang, X. Xu, X. Liu, Q. Yang, N. Shang, X. Zhao, X. Zang, C. Wang, Z. Wang, J.G. Shapter, Y. Yamauchi, Mater. Horiz. 9 (2022) 1708–1716.
[19] Z. Wang, J. Sun, B. Xu, Y. Liu, P. Ke, A. Wang, J. Eur. Ceram. Soc. 40 (2020) 197–201.
[20] J. Wang, T.-N. Ye, Y. Gong, J. Wu, N. Miao, T. Tada, H. Hosono, Nat. Commun. 10 (2019) 2284.
[21] N. Liu, J. Yuan, X. Zhang, Y. Ren, F. Yu, J. Ma, Mater. Horiz. 11 (2024) 1223–1233.
[22] L. Ma, L. Wei, M. Hamidinejad, C.B. Park, Mater. Horiz. 10 (2023) 4423–4437.
[23] C.L. Yeh, C.H. Chiang, Ceram. Int. 41 (2015) 6263–6268.
[24] S. Schweidler, M. Botros, F. Strauss, Q. Wang, Y. Ma, L. Velasco, G. Cadilha Marques, A. Sarkar, C. Kübel, H. Hahn, J. Aghassi-Hagmann, T. Brezesinski, B. Breitung, Nat. Rev. Mater. 9 (2024) 266–281.
[25] G. He, Y. Zhang, P. Yao, X. Li, K. Ma, J. Zuo, M. Li, C. Liu, J. Xu, J. Mater. Sci. Technol. 137 (2023) 91–99.
[26] H. Ding, Y. Li, M. Li, K. Chen, K. Liang, G. Chen, J. Lu, J. Palisaitis, P.O.Å. Persson, P. Eklund, L. Hultman, S. Du, Z. Chai, Y. Gogotsi, Q. Huang, Science 379 (2023) 1130–1135.
[27] L. Qiao, J. Bi, G. Liang, C. Liu, Z. Yin, Y. Yang, H. Wang, S. Wang, M. Shang, W. Wang, J. Mater. Sci. Technol. 137 (2023) 112–122.
[28] L. Fu, W. Xia, Adv. Eng. Mater. 23 (2021) 2001191.
[29] J. Lyu, E.B. Kashkarov, N. Travitzky, M.S. Syrtanov, A.M. Lider, J. Mater. Sci. 56 (2021) 1980–2015.
[30] Z. Wang, G. Ma, Z. Li, H. Ruan, J. Yuan, L. Wang, P. Ke, A. Wang, Corros. Sci. 192 (2021) 109788.
[31] M. Dahlqvist, M.W. Barsoum, J. Rosen. Mater. Today 72 (2024) 1–24.
[32] Z.M. Sun, Int. Mater. Rev. 56 (2011) 143–166.
[33] J.L. Lu, N. Abbas, J.N. Tang, J. Tang, G.M. Zhu, Corros. Sci. 158 (2019) 108106.
[34] L. Cai, Z. Huang, W. Hu, C. Lei, S. Wo, X. Li, H. Zhai, Y. Zhou, Int. J. Appl. Ceram. Technol. 15 (2018) 1212–1221.
[35] G. Wang, J. Zhou, W. Chen, J. Yang, J. Zhang, Y. He, Materials 14 (2021) 7068.
[36] C. Guo, E. Wang, S. Wang, X. Hou, Z. He, T. Liang, K.C. Chou, Corros. Sci. 180 (2021) 109197.
[37] S.J. Ouedraogo, Y. Vinh, P. Noophan, V. Naddeo, C.-W. Li, J. Clean. Prod. 404 (2023) 136987.
[38] R. Liu, Y. Xie, Y. Jin, Y. Cui, L. Liu, F. Wang, Acta Mater. 252 (2023) 118946.